Multiscale and Multidisciplinary Modeling, Experiments and Design (2023) 6:643–655
https://doi.org/10.1007/s41939-023-00166-9

ORIGINAL PAPER

Design of an ultra-small Wilkinson power divider using two-part resonators for S-band applications

Siyan Duan[1] · Juan Zhang[2] · Meijuan Liu[1]

Received: 30 March 2023 / Accepted: 19 May 2023 / Published online: 15 June 2023

Abstract

In this paper, a novel three-port Wilkinson power divider (WPD) with a compact size is designed and fabricated. New stepped impedance transmission lines, and two-part resonators between the input and output ports are used to suppress harmonics up to the ninth order and achieve a smaller size than a conventional power divider (75% size reduction) based on quarter-wavelength transmission lines. The characteristics of the transmission lines and resonators are obtained using an even and odd analysis. The results show that the S_{21} is about − 3.015 dB, the input return loss (S_{11}) is better than − 24 dB, and at a central frequency of 2.6 GHz, harmonics are eliminated as far as the 9th order.

Keywords Compact size · Harmonic suppression · Stepped impedance · Two-part resonators · Wilkinson power divider

1 Introduction

One of the essential circuits in telecommunication systems is power dividers (PDs) used in many components such as antennas, phase shifters, power amplifiers, etc. Usually, three-port networks have loss-matching networks. To solve this problem, the resistance between output ports is used to increase isolation. Conventional Wilkinson power divider has drawbacks such as low fractional bandwidth (FBW), large size, and inability to eliminate high-frequency harmonics. Researchers have recently tried to improve performance and reduce PD size (Pozar 2011; Zonouri and Hayati 2021; Imani et al. 2020; Pouryavar et al. 2018; Imani et al. 2019; Zhang et al. 2021a; Hayati et al. 2023; Jamshidi et al. 2021; Sattari et al. 2023; Roshani et al. 2021; Zonouri et al. 2023; Jedkare et al. 2020; Zhang et al. 2013; Li et al. 2017; Zonouri and Hayati 2019; Gai et al. 2017; Lin et al. 2017; Hosseini Tabatabaee et al. 2021; Li et al. 2016; Hao et al. 2023; Zhang et al. 2021b; Roshani et al. 2022; Wilkinson 1960; Zhuang et al. 2018; Zhang et al. 2018; Vaziri et al. 2020; Zhan and Zhao 2017; Tian and Dong 2022; Xiao et al. 2020).

✉ Siyan Duan
dsy440@126.com

1 School of Information Engineering, Yantai Institute of Technology, Yantai 264005, Shandong, China

2 Electronic Department, Yantai Automobile Engineering Professional College, Yantai 265500, Shandong, China

Different resonators and techniques are used in the PD structure, and different methods may be used to design these resonators, such as using a rectangular-shaped resonator (Pouryavar et al. 2018), triangular-shaped resonator (Imani et al. 2019), circular-shaped resonator (Zhang et al. 2021a) modified square resonator (Hayati et al. 2023), or a hybrid design technique (Jamshidi et al. 2021). The study of microstrip circuits has also attracted a lot of attention from academics in recent years, particularly with the use of intelligent approaches like GMDH neural networks (Sattari et al. 2023), multilayer perceptron network (Roshani et al. 2021) and the PSO optimization method (Zonouri et al. 2023).

Semicircular resonators in a symmetrical arrangement are utilized to provide small dimensions and a large pass-band in Jedkare et al. (2020). Nevertheless, the described structure uses spiral lines, making its implementation more difficult than it otherwise would be.

A small PD is introduced in Zhang et al. (2013). In this PD, the required transmission zeros are generated through the design of five resonators, but the high insertion losses and large size are the disadvantages of this design. A dual-band filtering WPD with multi-mode resonators is provided in Li et al. (2017), which can simultaneously divide the power and select the frequency, but suffers from a complex design structure. In (Zonouri and Hayati 2019), a low-pass WPD is provided with suppression of second to eighth-order harmonics with an attenuation level of 20 dB. The isolation at some points of the bandwidth is less than 10 dB.

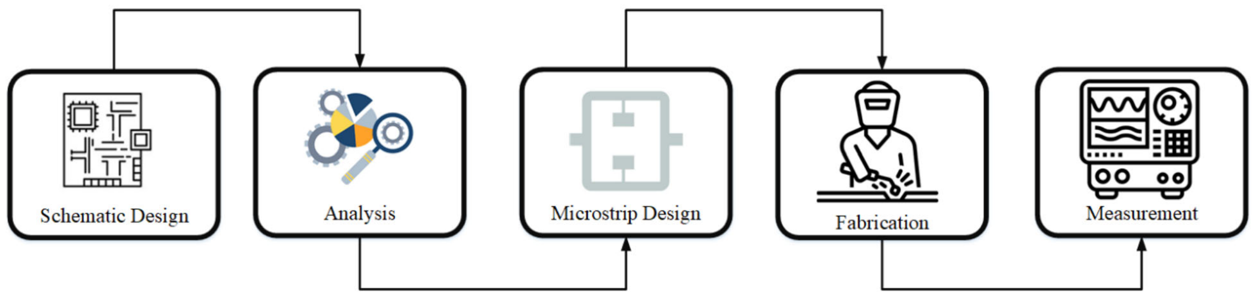

Fig. 1 Flowchart of the WPD design method

In (Gai et al. 2017), the uneven distribution of power is clearly shown. The transmission lines' length determines this PD. Any modification to the transmission lines will cause an arbitrary power split between the terminals. The operating frequency of this circuit is 2 GHz. An adjustable WPD is designed and fabricated in Lin et al. (2017). Coupled lines are used in its design. But the large dimensions of the circuit and the disregard for high-frequency harmonics are its weaknesses. In (Hosseini Tabatabaee et al. 2021), the transmission lines of a quarter of the wavelength are replaced by oval and rectangular resonators. The size of the circuit is reduced by about 55% compared to the conventional structure. It also has low insertion loss and attenuates unwanted harmonics. In (Li et al. 2016), a dual-band microstrip Gysel power divider is presented, simultaneously dividing the signal at two frequency bands and two-phase shifts. Transmission line characteristics can control the frequency bands. Also, two isolated and separate areas can be created between the frequency bands with two transmission lines connected to the output ports. As a result, a wide and isolated frequency band is created, and finally, the PD is made from the two presented dual-band structures.

Branch loading was employed in the coupled line in Hao et al. (2023), and by adding a stepped impedance open circuit stub, the filtering performance and pass-band bandwidth were improved, as was the stopband rejection performance. Also, in this structure, bending the microstrip line between the input and output parts has resulted in physical access to the isolation resistance and increased isolation performance between the output ports.

In (Zhang et al. 2021b), a PD is provided that uses a cascaded pair of couple line segments, each loaded with a half-wavelength open-circuit stub. The filter's bandwidth, selectivity, and band stop may all be enhanced by using half-wavelength open-circuit stubs. However, it has a huge size and a complex design.

As an alternative to the original PD branches, in ref Roshani et al. (2022) LC parts are combined together. The proposed new branches have produced a PD scheme that is small and meets the target miniaturization percentage.

Designing a PD with a compact size, low losses, and broad bandwidth remains challenging. To our knowledge, the microstrip WPD design based on two-part resonators has not been reported. Most of them are single-part and, of course, have limited efficiency.

In this paper, a modified Wilkinson power divider using new stepped impedance transmission lines and two-part resonators is designed and presented. Due to the two-part resonator structure, this PD can suppress unwanted harmonics using its wide stopband. It can remove as many as nine unwanted harmonics. Furthermore, it has an operating band with an FBW of 73.3%, which indicates its wide working band. The main novelty of this article is the design of a PD in which two-part and stepped impedance resonators are used, in its layout, for the first time with this geometry. On the other hand, the dimensions of the proposed PD have been reduced by more than 75% compared to the conventional circuit. The rest of the article is structured as follows: the second section details the designed WPD and the associated even and odd mode analysis. The implementation of the microstrip and resonators used is described in Sect. 3. Finally, simulation results and comparisons with previously reported works are discussed. In summary, the WPD design method can be seen in Fig. 1

2 Design of the stepped impedance WPD

2.1 Conventional WPD

The conventional WPD consists of two transmission lines, shown in Fig. 2. In this structure, each transmission line's characteristic impedance (Z0) and the electrical length (Θ) must be calculated. The conventional WPD consists of two transmission lines in which the characteristic impedance equals $\sqrt{2}\,Z_0$ (70.7 Ω), and the electrical length is 1/4 wavelength (90°) (Wilkinson 1960). The conventional WPD is a single frequency with relatively large dimensions, so it cannot be used in most radio frequency circuits today and must be modified.

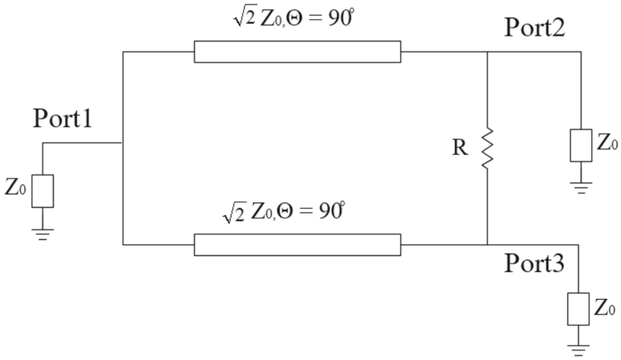

Fig. 2 Conventional WPD circuit diagram (Wilkinson 1960)

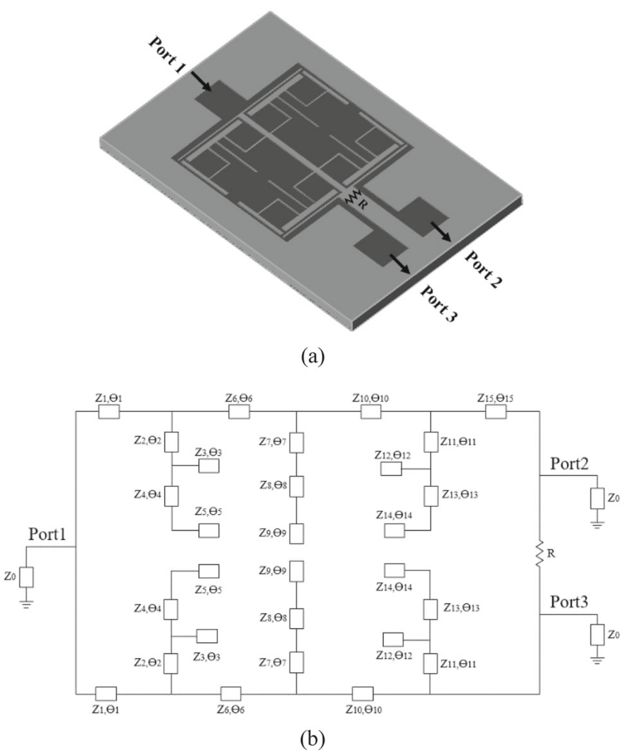

Fig. 3 **a** The physical 3D and **b** The equivalent circuit of the stepped impedance WPD

2.2 Stepped impedance circuit

Figure 3a shows the physical 3D circuit of the stepped impedance WPD, and Fig. 3b demonstrates the equivalent stepped impedance WPD circuit. Z_0 represents the impedance of the input and output ports, and R is the isolation resistance between the output ports (100 Ω). This design aims to calculate the optimal characteristic impedance of the odd and even mode for each section to reduce the return losses of all ports in the desired bandwidth.

2.3 Odd-mode analysis

In the odd-mode sub-structure, Z_{odd} is the equivalent impedance seen from the right, shown in Fig. 4. The odd-mode analysis is calculated step-by-step using the following equations:

$$Z_{o19} = jZ_1 tan\theta_1 \tag{1}$$

$$Z_{o18} = -jZ_5 cot\theta_5 \tag{2}$$

$$Z_{o17} = Z_4\left(\frac{Z_{o18} + jZ_4\tan\theta_4}{Z_4 + jZ_{o18}\tan\theta_4}\right) \tag{3}$$

$$Z_{o16} = \frac{Z_{o15}Z_{o14}}{Z_{o15} + Z_{o14}} \tag{4}$$

$$Z_{o14} = Z_2\left(\frac{Z_{o16} + jZ_2\tan\theta_2}{Z_2 + jZ_{o16}\tan\theta_2}\right) \tag{5}$$

Next, the impedance equivalent to the left branch of the circuit is calculated as follows:

$$Z_{o13} = \frac{Z_{o14}Z_{o19}}{Z_{o14} + Z_{o19}} \tag{6}$$

$$Z_{o12} = Z_6\left(\frac{Z_{o13} + jZ_6\tan\theta_6}{Z_6 + jZ_{o13}\tan\theta_6}\right) \tag{7}$$

$$Z_{o11} = -jZ_9 cot\theta_9 \tag{8}$$

$$Z_{o9} = Z_{o8}\left(\frac{Z_{o11} + jZ_8\tan\theta_8}{Z_8 + jZ_{o11}\tan\theta_8}\right) \tag{9}$$

$$Z_{o9} = Z_7\left(\frac{Z_{o10} + jZ_7\tan\theta_7}{Z_7 + jZ_{o10}\tan\theta_7}\right) \tag{10}$$

$$Z_{o8} = \frac{Z_{o9}Z_{o12}}{Z_{o9} + Z_{o12}} \tag{11}$$

$$Z_{o7} = Z_{10}\left(\frac{Z_{o8} + jZ_{10}\tan\theta_{10}}{Z_{10} + jZ_{o8}\tan\theta_{10}}\right) \tag{12}$$

$$Z_{o6} = -jZ_{14} cot\theta_{14} \tag{13}$$

$$Z_{o5} = Z_{13}\left(\frac{Z_{o6} + jZ_{13}\tan\theta_{13}}{Z_{13} + jZ_{o6}\tan\theta_{13}}\right) \tag{14}$$

$$Z_{o4} = \frac{Z_{o3}Z_{o2}}{Z_{o3} + Z_{o2}} \tag{15}$$

$$Z_{o2} = Z_{11}\left(\frac{Z_{o4} + jZ_{11}\tan\theta_{11}}{Z_{11} + jZ_{o4}\tan\theta_{11}}\right) \tag{16}$$

$$Z_{o1} = \frac{Z_{o7}Z_{o2}}{Z_{o7} + Z_{o2}} \tag{17}$$

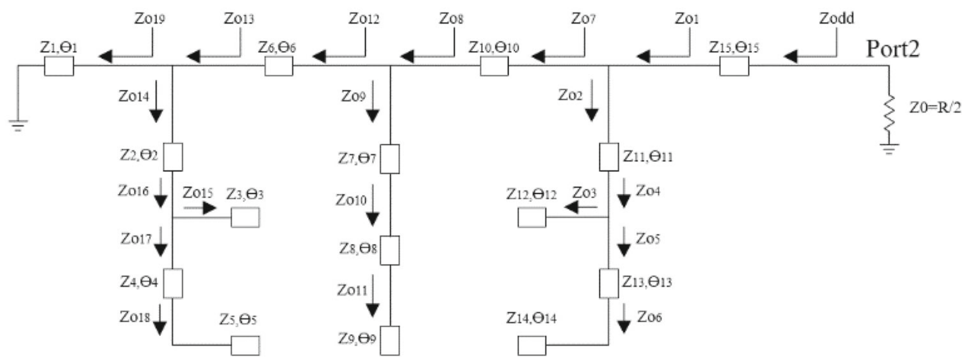

Fig. 4 Equivalent circuit for the odd mode

where Z_{odd} is the output impedance and could be obtained from (18):

$$Z_{odd} = Z_{15}\left(\frac{Z_{o1} + jZ_{15}\tan\theta_{15}}{Z_{15} + jZ_{o1}\tan\theta_{15}}\right) \tag{18}$$

Based on (18), the derived reflection coefficient Γ_{out}^{odd} in the output ports is calculated as follows:

$$\Gamma_{out}^{odd} = \frac{Z_{odd} - Z_o}{Z_{odd} + Z_o} \tag{19}$$

In this design, like in the conventional WPD structure, the real part of *Zo* is equal to 50 Ω, and the imaginary part equals zero. Also, the isolation resistance is 100 Ω.

2.4 Even-mode analysis

In the even mode, as shown in Fig. 5, no current flows through resistors *R* or between the inputs of two transmission lines on port 1. Z_{even} is the equivalent impedance, which can be calculated as follow:

$$Z_{e19} = Z_{15}\left(\frac{Z_o + jZ_{15}\tan\theta_{15}}{Z_{15} + jZ_o\tan\theta_{15}}\right) \tag{20}$$

$$Z_{e18} = -jZ_{14}\cot\theta_{14} \tag{21}$$

$$Z_{e17} = Z_{13}\left(\frac{Z_{e18} + jZ_{13}\tan\theta_{13}}{Z_{13} + jZ_{e18}\tan\theta_{13}}\right) \tag{22}$$

$$Z_{e16} = -jZ_{12}\cot\theta_{12} \tag{23}$$

$$Z_{e15} = \frac{Z_{e17}Z_{e16}}{Z_{e17} + Z_{e16}} \tag{24}$$

$$Z_{e17} = Z_{11}\left(\frac{Z_{e15} + jZ_{11}\tan\theta_{11}}{Z_{11} + jZ_{e15}\tan\theta_{11}}\right) \tag{25}$$

Next, the impedance equivalent to the right branch of the equivalent circuit is obtained as follows:

$$Z_{e13} = \frac{Z_{e19}Z_{e14}}{Z_{e19} + Z_{e14}} \tag{26}$$

$$Z_{e12} = Z_{10}\left(\frac{Z_{e13} + jZ_{10}\tan\theta_{10}}{Z_{10} + jZ_{e13}\tan\theta_{10}}\right) \tag{27}$$

$$Z_{e10} = Z_8\left(\frac{Z_{e11} + jZ_8\tan\theta_8}{Z_8 + jZ_{e11}\tan\theta_8}\right) \tag{29}$$

$$Z_{e9} = Z_7\left(\frac{Z_{e10} + jZ_7\tan\theta_7}{Z_7 + jZ_{e9}\tan\theta_7}\right) \tag{30}$$

$$Z_{e8} = \frac{Z_{e12}Z_{e9}}{Z_{e12} + Z_{e9}} \tag{31}$$

$$Z_{e7} = Z_6\left(\frac{Z_{e8} + jZ_6\tan\theta_6}{Z_6 + jZ_{e8}\tan\theta_6}\right) \tag{32}$$

$$Z_{e6} = -jZ_5\cot\theta_5 \tag{33}$$

$$Z_{e5} = Z_4\left(\frac{Z_{e6} + jZ_4\tan\theta_4}{Z_4 + jZ_{e6}\tan\theta_4}\right) \tag{34}$$

$$Z_{e4} = \frac{Z_{e2}Z_{e3}}{Z_{e2} + Z_{e3}} \tag{35}$$

$$Z_{e3} = -jZ_3\cot\theta_3 \tag{36}$$

$$Z_{e2} = Z_2\left(\frac{Z_{e3} + jZ_2\tan\theta_2}{Z_2 + jZ_{e3}\tan\theta_2}\right) \tag{37}$$

$$Z_{e1} = \frac{Z_{e7}Z_{e2}}{Z_{e7} + Z_{e2}} \tag{38}$$

where Z_{even} is the input impedance on the left side of Fig. 5 and can be shown as:

$$Z_{even} = Z_1\left(\frac{Z_{e1} + jZ_1\tan\theta_1}{Z_1 + jZ_{e1}\tan\theta_1}\right) \tag{39}$$

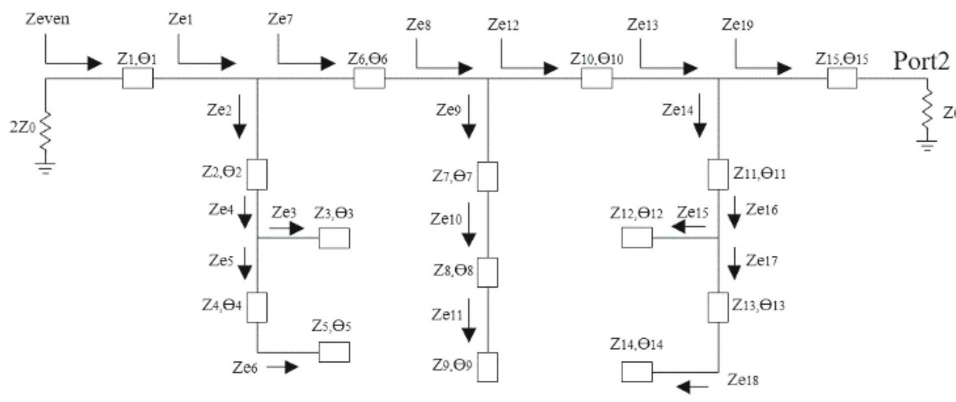

Fig. 5 Equivalent circuit for the even mode

According to (39), the reflection coefficient derived at the input port or parameter S_{11} can be obtained as follows:

$$S_{11} = \Gamma_{in}^{even} = \frac{Z_{even} - 2Z_o}{Z_{even} + 2Z_o} \tag{40}$$

So, due to the physical limitation in the implementation of the WPD, Z_1, and Z_6 are selected to be 168 and 160 Ω, respectively.

2.5 Parameters of the stepped impedance WPD

In the presented structure, the isolation between the output ports of the WPD is considered zero ($S_{23} = 0$) and is symmetric for simplicity as well. Therefore, $Z_1 = Z_{15}$, $Z_6 = Z_{10}$, $Z_2 = Z_{11}$, $Z_2 = Z_{11}$, $Z_3 = Z_{12}$, $Z_4 = Z_{13}$, and $Z_5 = Z_{14}$.

In the operating band of the stepped impedance WPD, the return loss is assumed to be greater than 15 dB. Furthermore, in the conventional structure, the characteristic impedance of each transmission line is 70.7Ω, so all the impedances and electrical lengths of the stepped impedance structure can be obtained according to Table 1 (Units are Z, Ω, $\theta°$).

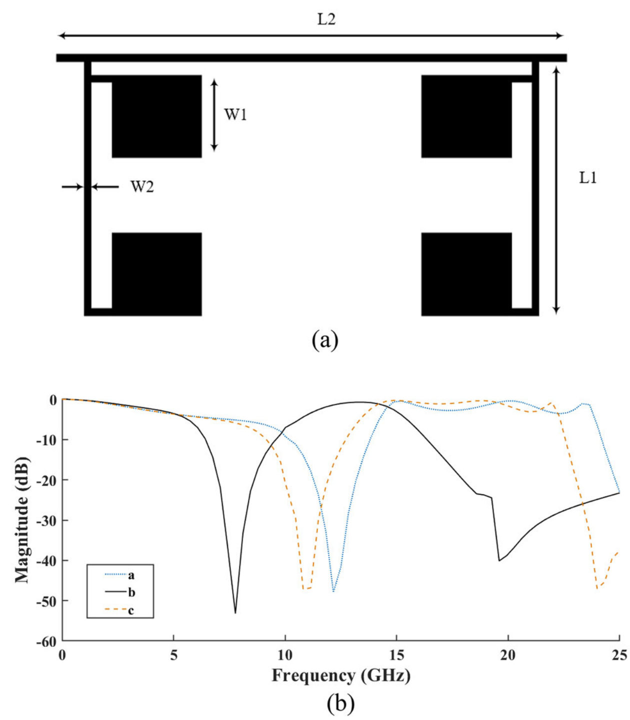

Fig. 6 **a** The layout, and **b** The simulated S_{12} of proposed two-part resonators in different dimensions

3 Microstrip WPD design

The proposed stepped impedance WPD design approach implements a microstrip waveguide. Microstrip technology is a good choice for implementing microwave filters, power dividers, and couplers. The advantages of using microstrip lines include compact size, low cost, easy fabrication, lightweight, and the ability to integrate them with other microwave circuit elements on a circuit board. Therefore, to implement the stepped impedance circuit, microstrip stubs and resonators are used, in which impedances two-part resonators replace Z_2 to Z_5 and Z_{11} to Z_{14}. Stepped impedance resonators substitute the impedances Z_7 to Z_9.

3.1 Two-part resonators

According to Fig. 6a, two-part resonators have implemented symmetric impedances Z_2 to Z_5 and Z_{11} to Z_{14}. In the presented design, the sizes of L2 and W2 are 7.4 and 0.1 mm, respectively, and the result of insertion losses (S_{21}) for dimensions (a) L1 = 3.5 mm, W1 = 1.2 mm, (b) L1 = 3.7 mm, W1 = 1.2 mm, and (c) L1 = 3.7 mm, W1 = 1 mm is simulated in Fig. 6b. The simulation results show that the condition of mode (b) produces the best output response because it has produced two transmission zeros with the lowest level of attenuation and compared to mode (a) and (c), it has a better bandwidth.

Table 1 Calculated parameters of the stepped impedance circuit

Z_1	θ_1	Z_2	θ_2	Z_3	θ_3	Z_4	θ_4
168	1.5	167.5	2	56.2	6.5	158	14.3
$\mathbf{Z_5}$	$\boldsymbol{\theta_5}$	$\mathbf{Z_6}$	$\boldsymbol{\theta_6}$	$\mathbf{Z_7}$	$\boldsymbol{\theta_7}$	$\mathbf{Z_8}$	$\boldsymbol{\theta_8}$
56.2	6.5	160	11.7	31	5.6	18.2	4
$\mathbf{Z_9}$	$\boldsymbol{\theta_9}$	$\mathbf{Z_{10}}$	$\boldsymbol{\theta_{10}}$	$\mathbf{Z_{11}}$	$\boldsymbol{\theta_1}$	$\mathbf{Z_{12}}$	$\boldsymbol{\theta_{12}}$
41	7.6	160	11.7	167.5	2	56.2	6.5
$\mathbf{Z_{13}}$	$\boldsymbol{\theta_{13}}$	$\mathbf{Z_{14}}$	$\boldsymbol{\theta_{14}}$	$\mathbf{Z_{15}}$	$\boldsymbol{\theta_{15}}$	**R**	
158	14.3	56.2	6.5	168	1.5	100	

Figure 7a depicts the LC equivalent circuit of the two-part resonators. Following the method outlined in Refs. (Imani et al. 2020; Pouryavar et al. 2018), the inductor and capacitor values can be determined.

Each microstrip line in the LC model can be thought of as a series inductor and a grounded capacitor. From this, the equivalent L-C circuit can be formed. The following set of equations can be used to accurately simulate transmission lines (Pozar 2011):

$$C = \left[8.85 \times 10^{-12} \left\{ \left[\frac{\varepsilon_r \times w}{h}\right]^{1.08} + \left[2\pi\left(\frac{\varepsilon_r + 1}{2}\right)\left(\frac{1}{\ln\left(\frac{8h}{w} + 1\right)} - \frac{w}{8h}\right)\right]^{1.08} \right\}^{0.926}\right] \times l \tag{41}$$

$$L = \frac{Z \times l}{V_p},\ V_p = \frac{c}{\sqrt{\varepsilon_{re}}} \tag{42}$$

For $w/h \leq 1$:

$$\varepsilon_{re} = \frac{\varepsilon_r + 1}{2} + \frac{\varepsilon_r - 1}{2}\left\{\left[1 + 12\frac{h}{w}\right]^{-0.5} + 0.04\left[1 - \frac{w}{h}\right]^2\right\},\ Z = \frac{\eta}{2\pi\sqrt{\varepsilon_{re}}}\ln\left[8\frac{h}{w} + 0.25\frac{w}{h}\right] \tag{43}$$

For $w/h \geq 1$:

$$\varepsilon_{re} = \frac{\varepsilon_r + 1}{2} + \frac{\varepsilon_r - 1}{2}\left\{\left[1 + 12\frac{h}{w}\right]^{-0.5}\right\},\ Z = \frac{\eta}{\sqrt{\varepsilon_{re}}}\left\{\frac{h}{w} + 1.393 + 0.677\ln\left[\frac{w}{h} + 1.444\right]\right\}^{-1} \tag{44}$$

where Z is the transmission line's characteristic impedance and Vp is its phase velocity. Light velocity is given by c, and is a constant quantity equal to 377 (120π) Ω; l is the length of the transmission line; w and h are the line width and substrate thickness, respectively. Table 2 lists the capacitor and inductor values used in the circuit seen in Figs. 7a and 9a.

Based on Fig. 7a, we may infer that the impedance seen from Va and Vb is Zb, Zc, and derive the transfer function as:

$$\frac{V_a}{L_1 \times S + 50} = \frac{V_i}{50} \tag{45}$$

$$V_a = \frac{(L_1 \times S + 50)V_i}{50} \tag{46}$$

$$\frac{V_b}{L_3 \times S + 50} = \frac{V_o}{50} \tag{47}$$

$$V_b = \frac{(L_3 \times S + 50)V_o}{50} \tag{48}$$

Table 2 The values of inductors and capacitors Figs. 7a and 9a (all values are in pF and nH)

L_1	L_2	L_3	L_4	L_5	L_6	L_7	L_8	L_9	L_{10}	L_{11}	L_{12}	L_{13}	L_{14}
2.5	7.71	2.5	3	0.3	2.4	0.3	3	0.3	2.4	0.3	6.5	0.4	0.25
C_1	C_2	C_3	C_4	C_5	C_6	C_7	C_8	C_9	C_{10}	C_{11}	C_{12}	C_{13}	
0.15	0.134	0.48	0.48	0.55	0.55	0.74	0.74	0.55	0.55	0.146	0.78	0.78	

Both Eq. (45) and (46) assume a matched impedance of 50 O between the input and output ports in their calculations. Assuming Va and Vb are nodes, we now have:

$$\frac{V_a - V_i}{L_1 \times S} + \frac{V_a}{Z_b} + \frac{V_b - V_a}{L_2 \times S} + \frac{V_b}{Z_c} + \frac{V_o - V_b}{L_3 \times S} = 0 \tag{49}$$

where

$$Z_b = \left(\left(\left(\left(\left(\left(\frac{1}{C_9 \times S} + L_7 \times S\right) || \frac{1}{C_7 \times S}\right) + L_6 \times S\right) || \frac{1}{C_5 \times S} + L_5 \times S\right) || \frac{1}{C_3 \times S} + L_4 \times S\right) || \frac{1}{C_1 \times S} + L_1 \times S\right) \tag{50}$$

$$Z_c = \left(\left(\left(\left(\left(\left(\frac{1}{C_{10} \times S} + L_{11} \times S\right) || \frac{1}{C_8 \times S}\right) + L_{10} \times S\right) || \frac{1}{C_6 \times S} + L_9 \times S\right) || \frac{1}{C_4 \times S} + L_8 \times S\right) || \frac{1}{C_2 \times S} + L_3 \times S\right) \tag{51}$$

From Eq. (46), (48) and Eq. (49), the transfer function of V_o and V_i can be written as:

$$\frac{V_o}{V_i} = \frac{50 \times Z_b \times Z_c}{(L_1 \times S + 2 \times Z_b)(50 + L_1 \times S)(L_3 \times S + 2 \times Z_c)(50 + L_3 \times S) - (50 \times Z_b)(50 \times Z_c)} \tag{52}$$

Setting Eq. (52) to zero gives us the transmission zeros, thus we have:

$$f_{zero3} = 7.82GHz$$

$$f_{zero4} = 19.9GHz$$

As seen from the frequency simulation result of this structure with the dimensions of mode b in Fig. 7b, these resonators produce two transmission zeros (TZs) at a frequency of 7.9 GHz and 19.8 GHz, respectively. These novel resonators with long bases and two parts are designed to occupy a small space while creating TZ. Therefore, it can be concluded that the simulation results of the LC equivalent circuit with the layout are slightly different from each other.

3.2 Stepped impedance resonators

To increase the stopband bandwidth of the PD, another resonator is added to the microstrip circuit, as shown in Fig. 8a. Figure 3 shows this resonator consists of three different transmission lines whose impedances vary step by step. According to Fig. 8a, L3 and W4 are 1.3 and 0.4 mm, respectively. Also, the response of S_{12} for different W5/W3 ratios is simulated in Fig. 8b. The created transmission zeros can easily be moved by changing the dimensions of the resonator. For W5/W3 = 4.2, the most optimal result is obtained because two transmission zeros are obtained in the response, which has a better attenuation rate compared to others, and also reaches the highest level in the passband.

The LC equivalent circuit of the stepped impedance resonator is shown in Fig. 9a. Based on Fig. 9a, we may infer that the impedance seen from V_x is Z_a, and derive the transfer function as:

$$\frac{V_x}{L_{12} \times S + 50} = \frac{V_o}{50} \tag{53}$$

$$V_x = \frac{(L_{12} \times S + 50)V_o}{50} \tag{54}$$

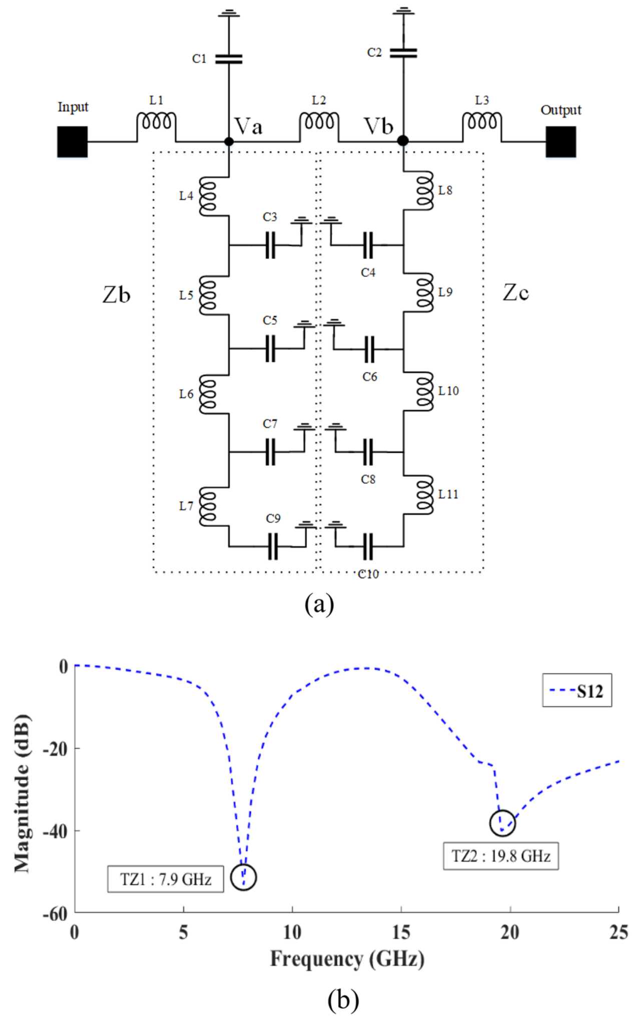

Fig. 7 **a** L-C Equivalent. **b** The simulated S_{12} of proposed two-part resonators for the dimensions of mode (**b**)

Equation (53) assumes a matched impedance of 50 O between the input and output ports in their calculations. Assuming V_x is a node, we now have:

$$\frac{V_x - V_i}{L_1 \times S} + \frac{V_x}{Z_x} + \frac{V_x - V_o}{L_1 \times S} = 0 \tag{55}$$

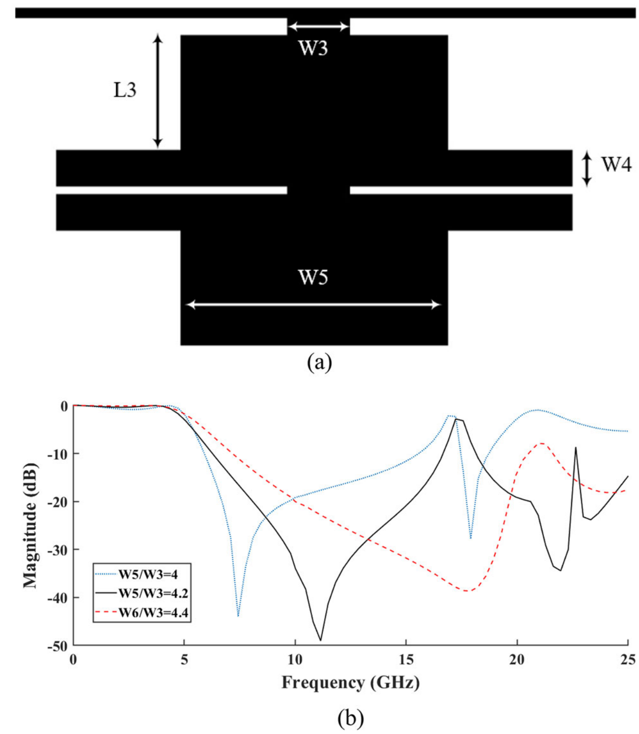

Fig. 8 **a** The layout, and **b** The simulated S_{12} of stepped impedance resonators in different dimensions

where

$$Z_a = (((((\frac{1}{C_{13} \times S} + L_{14} \times S) \| \frac{1}{C_{12} \times S}) + L_{13} \times S) \| \frac{1}{C_{11} \times S}) + L_{12} \times S) \tag{56}$$

From Eq. (54) and Eq. (55), the transfer function of Vo and Vi can be written as:

$$\frac{V_o}{V_i} = \frac{50 \times Z_a}{(L_{12} \times S + 2 \times Z_a)(50 + L_{12} \times S) - (50 \times Z_a)} \tag{57}$$

Setting Eq. (57) to zero gives us the transmission zeros, thus we have:

$$f_{zero1} = \frac{\sqrt{\frac{1}{C_{12}L_{13}} + \frac{1}{C_{12}L_{14}} + \frac{1}{C_{13}L_{14}} + \frac{-4C_{12}C_{13}L_{13}L_{14} + (C_{12}L_{13} + C_{12}L_{14} + C_{13}L_{14})^2}{C_{12}C_{13}L_{13}L_{14}}}}{2\pi\sqrt{2}} \tag{58}$$

$$f_{zero2} = \frac{\sqrt{\frac{1}{C_{12}L_{13}} + \frac{1}{C_{12}L_{14}} + \frac{1}{C_{13}L_{14}} - \frac{-4C_{12}C_{13}L_{13}L_{14} + (C_{12}L_{13} + C_{12}L_{14} + C_{13}L_{14})^2}{C_{12}C_{13}L_{13}L_{14}}}}{2\pi\sqrt{2}} \tag{59}$$

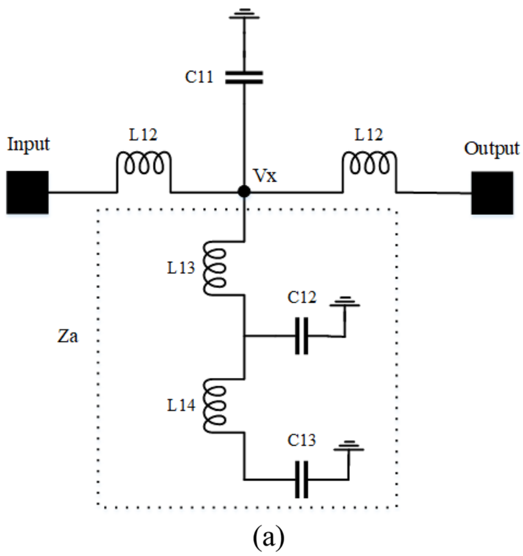

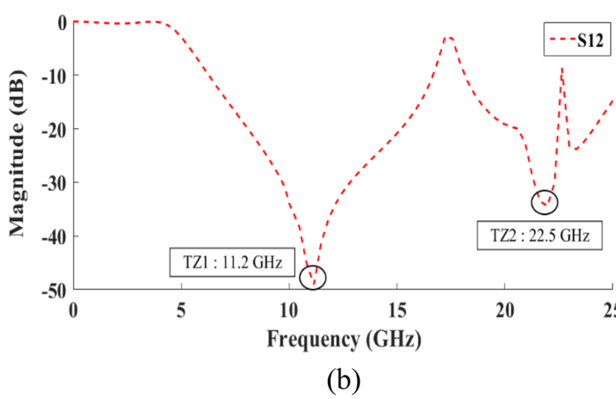

Fig. 9 **a** L-C Equivalent. **b** The simulated S_{12} of proposed stepped impedance resonators for W5/W3 = 4.2

Using the values of capacitors and inductors of Table 2, the cut-off frequencies in Eq. (58) and (59) are evaluated as:

$$f_{zero1} = 11.16GHz$$

$$f_{zero2} = 22.45GHz$$

According to Fig. 9b, this resonator also creates two TZs at a frequency of 11.2 GHz and 22.5 GHz, respectively. These frequencies are the resonance frequencies of the proposed resonator in Fig. 8a. As the layout simulation results show, the LC equivalent circuit analysis results are very close to each other compared to the simulation and have little difference, which shows the high validity of the calculated results.

3.3 Final structure

According to Fig. 10, the final structure of the proposed WPD is formed by combining the two-part with the stepped impedance resonators. This compact structure is symmetrical on the vertical axis, so it can be easily fabricated using microstrip technology. On the other hand, the equivalent impedance is equal to the impedance of each branch of the conventional WPD.

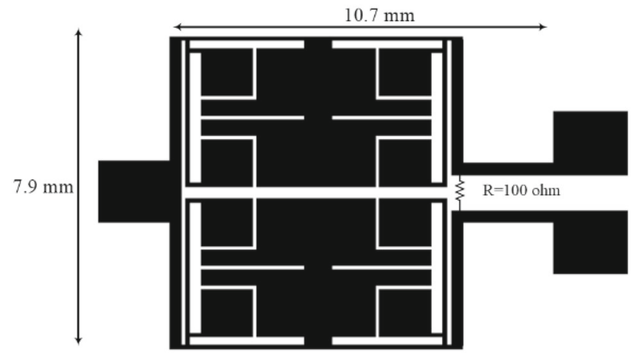

Fig. 10 The layout of the final WPD structure

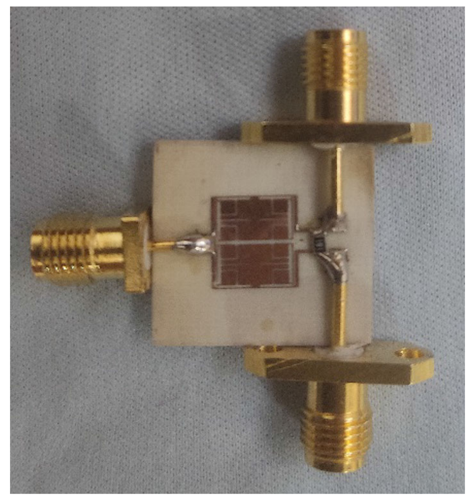

Fig. 11 Fabricated WPD

4 Simulation and fabrication results

The wide-band WPD is simulated on a Rogers RO4003 substrate with a thickness of 0.508 mm and a relative dielectric constant of 0.0022 using electromagnetic wave simulator software (ADS). The circuit's overall size equals 7.4 mm × 7.9 mm (0.106 λ_g × 0.114 λ_g). The photograph of the fabricated WPD is shown in Fig. 11. This circuit has an 75% reduction in dimensions compared to the conventional structure. Where λ_g is (Zonouri and Hayati 2019):

$$\lambda_g = \frac{300}{f(GHz) \times \sqrt{\varepsilon_{re}}}(\text{mm}) \quad (60)$$

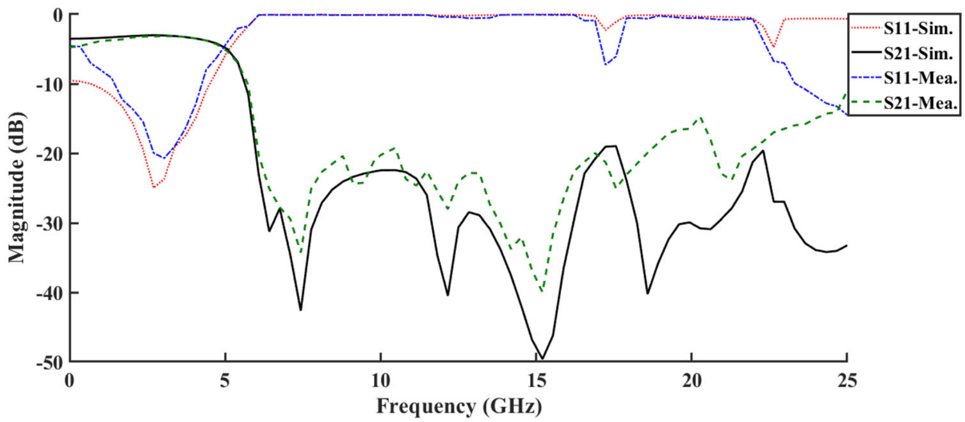

Fig. 12 Results of the measured and simulated return and insertion losses at the input port

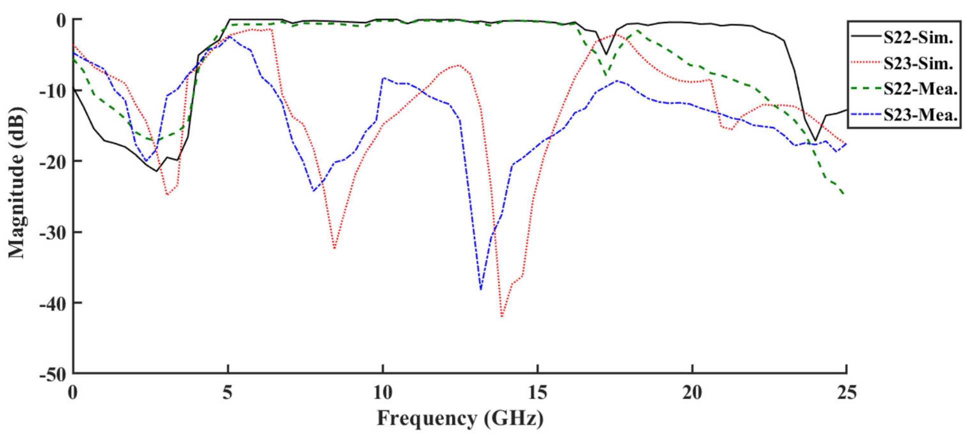

Fig. 13 Results of the measured and simulated return and insertion losses at the output port

where ε_{re} is the microstrip line's effective dielectric constant.

Furthermore, the simulation and measurement results of S-parameters are shown in Figs. 12 and 13. As expected, there is a slight difference between the simulation result and the fabrication due to fabrication and soldering errors.

As can be seen, this single-band WPD at 2.6 GHz has an insertion loss of − 3.015 dB and fluctuates very little throughout the bandwidth.

According to Fig. 12, the proposed structure has a return loss of less than − 15 dB in the bandwidth, and S11 is equal to − 24 dB at the central frequency.

According to $S_{11} = -15$ dB, the bandwidth is from 1.6 to 3.5 GHz, while the center frequency of 2.6 GHz. Since the bandwidth of the proposed power divider ranges from 1.6 GHz to 3.5 GHz and the center frequency is 2.6 GHz, FBW is calculated as follows (Zonouri and Hayati 2019):

$$FBW\% = \frac{B.W}{f_0} \times 100 = \frac{3.5GHz - 1.6GHz}{2.6GHz} = 73.3\% \tag{61}$$

The simulation results of return losses at the output port (S_{22}–S_{33}) and isolation between ports 2 and 3 (S_{23}) are shown

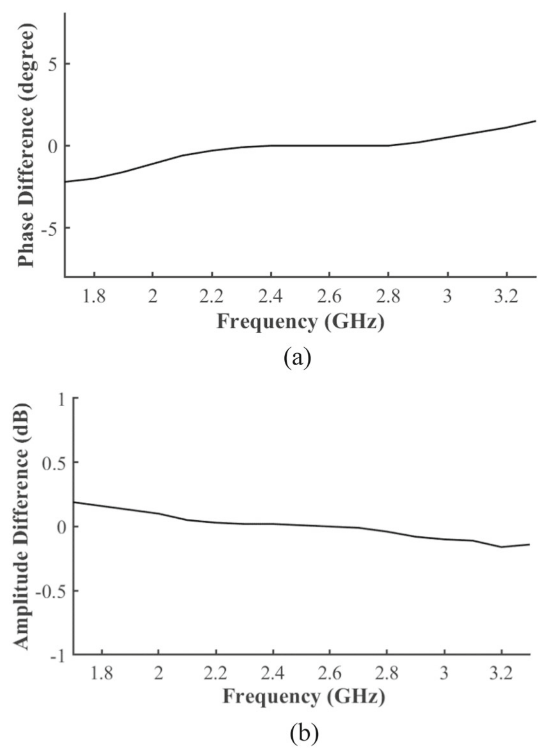

Fig. 14 **a** The phase and **b** the amplitude difference between output ports

Table 3 Comparison with previously reported works

References	Operating frequency (GHz)	FBW (%)	Return loss (dB)	Technique	Insertion loss (dB)	Size ($\lambda_g \times \lambda_g$)	Harmonic suppression
Imani et al. 2020)	1.1	–	− 16.6	Comb-shaped resonators	− 3.5	0.06 × 0.07	3rd–10th
Pouryavar et al. 2018)	1.95	50	− 15	Radial/rectangular-shaped resonators	–	0.12 × 0.10	3rd–8th
Imani et al. 2019)	2.5	–	− 35	Triangular shaped resonator	− 3.6	0.06 × 0.08	3rd–11th
Roshani et al. 2021)	1.9	–	− 42	T-shaped resonators—artifcial neural network	–	0.1 × 0.07	2nd–4th
Zonouri and Hayati 2019)	1.65	68	− 20	Trapezoidal and triangular-shaped resonators	− 3.02	0.066 × 0.069	2nd–8th
Hao et al. 2023)	2.85	52.9	− 20	Step impedance open-circuit stub	− 3.62	0.41 × 0.47	2nd–4th
Zhang et al. 2021b)	1.75	62.3	− 20	Two cascaded coupled-line	− 3.3	0.4 × 0.3	2nd–4th
Roshani et al. 2022)	0.9	–	− 20	Resonant LC Branches	− 3.3	very small	2nd–45th
Zhuang et al. 2018)	2	51	− 15	Open-circuit stubs	− 3.6	0.88 × 0.88	2nd
Zhang et al. 2018)	2.2	18.2	− 19.5	Co-shared single resistor	− 3.95	0.32 × 0.32	2nd–3rd
Vaziri et al. 2020)	2.45	8.2	− 17	Elliptic-shaped resonator	− 3.2	0.28 × 0.28	2nd–8th
Zhan and Zhao 2017)	2.4	28	− 20	Stub-loaded resonator	− 3.8	0.15 × 0.19	2nd–3rd
Tian and Dong 2022)	2.45	19.6	− 19.5	Parallel-coupled lines	− 3.59	0.25 × 0.38	2nd–3rd
Xiao et al. 2020)	3.9	63.6	− 24	Self-packaged SISL technologies	− 3.74	0.29 × 0.47	2nd
This work	2.6	73.3	− 24	Two-part Resonators	− 3.015	0.114 × 0.106	2nd–9th

in Fig. 13. If we set the − 20 dB level as a comparison level, then this circuit has a wide stopband, in which it suppresses nine unwanted harmonics with the level of attenuation -20.5, 35.1, − 23.2, − 34.3, − 30.7, − 37.4, − 29.1, − 22.8, and − 31.1 dB, respectively.

In a PD, the input signal is divided into two output signals with the same amplitude. Still, there may be slight variations in the amplitude of the signals relative to each other, and the output signals have phase differences. Figure 14a, b depict the phase and amplitude variances between the output ports, respectively. The phase and amplitude differences are lower than 1.5° and less than 0.2 dB in the pass-band. Therefore, the proposed structure has an equal power division at the output ports and is symmetric.

Table 3 compares the proposed WPD's performance to that of comparable works. As can be seen, the simulated performance of the proposed structure outperforms other solutions in terms of insertion losses, FBW, return losses, technique and harmonic suppression. Also, the circuit size is smaller than most previous works and has a simpler structure. To put it simply, it excels at S-band uses. The presented circuit has the best FBW and insertion loss compared to other works, which makes its applications wider. Hence, the developed circuit has applications in airport radars for air traffic management, weather surveillance radar, and several telecommunication networks.

5 Conclusion

This article proposes a novel compact broadband WPD using microstrip lines at a central frequency of 2.6 GHz to improve the previous solutions using a novel two-part and stepped impedance resonator. The even and odd mode method has been used to analyze the designed circuit. The simulation results show that nine unwanted harmonics are suppressed. The FBW is 73.3%, and the circuit size is just 0.106 $\lambda_g \times 0.114\ \lambda_g$. The above properties make the designed WPD attractive for applications in microwave amplifiers for dividing or coupling power, antenna arrays, and mixers.

Author contributions SD: writing-original draft preparation, conceptualization, supervision, project administration. JZ: software, validation, formal analysis, language review. ML: methodology, writing-original draft preparation, software, language review.

Declarations

Conflict of interest The authors declare no competing of interests.

References

Gai C, Jiao YC, Weng ZB, Zhao G, Zhao YL (2017) Dual band gysel power divider with high power dividing ratio. Microw Opt Technol Lett 59(10):2428–2431

Hao H, Xu H, Ling Q, Wang Y (2023) Design of a planar filtering power divider with wide-stopband suppression. Electromagnetics:1–10.

Hayati M, Sattari MA, Zarghami S, Shah-ebrahimi SM (2023) Designing ultra-small Wilkinson power divider with multi-harmonics suppression. J Electromagn Waves Appl 37(4):575–591

Hosseini Tabatabaee A, Shama F, Sattari MA, Veysifard S (2021) A miniaturized Wilkinson power divider with 12th harmonics suppression. J Electromagn Waves Appl 35(3):371–388

Imani MA, Shama F, Alirezapoori M, Haghiri S, Ghadrdan A (2019) Ultra-miniaturized Wilkinson power divider with harmonics suppression for wireless applications. J Electromagn Waves Appl 33(14):1920–1932

Imani MA, Shama F, Roshani GH (2020) Miniaturized Wilkinson power divider with suppressed harmonics. Microw Opt Technol Lett 62(4):1526–1532

Jamshidi MB, Roshani S, Talla J, Roshani S, Peroutka Z (2021) Size reduction and performance improvement of a microstrip Wilkinson power divider using a hybrid design technique. Sci Rep 11(1):7773

Jedkare E, Shama F, Sattari MA (2020) Compact Wilkinson power divider with multi-harmonics suppression. AEU Int J Electron Commun 127:153436

Li J, Zhou H, Ma Q, Chai Y, Yan K (2016) Planar power divider with arbitrary power ratio for high power application and its miniaturization. In: 2016 IEEE International Conference on Microwave and Millimeter Wave Technology (ICMMT), vol. 1, pp. 238–240

Li Q, Zhang Y, Wu CTM (2017) High-selectivity and miniaturized filtering Wilkinson power dividers integrated with multimode resonators. IEEE Trans Compt, Packag Manufact Technol 7(12):1990–1997

Lin SC, Chen YM, Chiou PY, Chang SF (2017) Tunable Wilkinson power divider utilizing parallel-coupled-line-based phase shifters. IEEE Microw Wirel Compon Lett 27(4):335–337

Pouryavar R, Shama F, Imani MA (2018) A miniaturized microstrip Wilkinson power divider with harmonics suppression using radial/rectangular-shaped resonators. Electromagnetics 38(2):113–122

Pozar DM (2011) Microwave engineering. Wiley

Roshani S, Jamshidi MB, Mohebi F, Roshani S (2021) Design and modeling of a compact power divider with squared resonators using artificial intelligence. Wirel Pers Commun 117:2085–2096

Roshani S, Yahya SI, Alameri BM, Mezaal YS, Liu LW, Roshani S (2022) Filtering power divider design using resonant LC branches for 5G low-band applications. Sustainability 14(19):12291

Sattari MA, Hayati M, Shama F, Shah-Ebrahimi SM (2023) A miniaturized filter design approach using GMDH neural networks. Microw Opt Technol Lett. https://doi.org/10.1002/mop.33741

Tian H, Dong Y (2022) Packaged Filtering power divider with high selectivity, extended stopband and wide-band isolation. IEEE Trans Circ Syst II Express Briefs

Vaziri HS, Zarghami S, Shama F, Kazemi AH (2020) Compact bandpass Wilkinson power divider with harmonics suppression. AEU Int J Electron Commun 117:153107

Wilkinson EJ (1960) An N-way hybrid power divider. IRE Trans Microw Theory Tech 8(1):116–118

Xiao JK, Yang XY, Li XF (2020) A 3.9 GHz/63.6% FBW multi-mode filtering power divider using self-packaged SISL. IEEE Trans Circ Syst II Express Briefs 68(6):1842–1846

Zhan WL, Zhao XL (2017) Compact filtering power divider with harmonic suppression. J Electromagn Waves Appl 31(3):243–249

Zhang XY, Wang KX, Hu BJ (2013) Compact filtering power divider with enhanced second-harmonic suppression. IEEE Microw Wirel Compon Lett 23(9):483–485

Zhang G, Wang X, Hong JS, Yang J (2018) A high-performance dualmode filtering power divider with simple layout. IEEE Microw Wirel Compon Lett. 28(2):120–122

Zhang Q, Zhang G, Liu Z, Chen W, Tang W (2021a) Dual-band filtering power divider based on a single circular patch resonator with improved bandwidths and good isolation. IEEE Trans Circuits Syst II Express Briefs 68(11):3411–3415

Zhang Y, Wu Y, Yan J, Wang W (2021b) Wide-band high-selectivity filtering all-frequency absorptive power divider with deep out-of-band suppression. IEEE Trans Plasma Sci 49(7):2099–2106

Zhuang Z, Wu Y, Liu Y, Ghassemlooy Z (2018) Wide-band bandpass-to-all-stop reconfigurable filtering power divider with bandwidth control and all-passband isolation. IET Microw Anten Propag 12(11):1852–1858

Zonouri SA, Hayati M (2019) A compact ultra-wideband Wilkinson power divider based on trapezoidal and triangular-shaped resonators with harmonics suppression. Microelectron J 89:23–29

Zonouri SA, Hayati M (2021) A compact Gysel power divider with ultra-wide rejection band and high fractional bandwidth. Int J RF Microw Comput Aided Eng 31(6):e22643

Zonouri SA, Hayati M, Bahrambeigi M (2023) Design of dual-band Wilkinson power divider based on novel stubs using PSO algorithm. Int J Microw Wirel Technol:1–12.